

Supplementary Materials for
**Suppressed Size Effects in Nanopillars with Hierarchical Microstructures
Enabled by Nanoscale Additive Manufacturing**

Wenxin Zhang^{1†*}, Zhi Li^{2†}, Ruoqi Dang^{2,3}, Thomas T. Tran¹, Rebecca A. Gallivan^{1,4}, Huajian Gao^{2,3},
Julia R. Greer^{1,5}

¹Division of Engineering and Applied Sciences, California Institute of Technology, 1200 E. California Blvd., Pasadena, CA 91125, U.S.A.

²Institute of High Performance Computing, A*STAR, 138632, Singapore.

³School of Mechanical and Aerospace Engineering, College of Engineering, Nanyang Technological University, 70 Nanyang Drive, 639798, Singapore.

⁴Laboratory for Nanometallurgy, Department of Materials, ETH Zürich, 8093 Zürich, Switzerland

⁵Kavli Nanoscience Institute, California Institute of Technology, 1200 E. California Blvd., Pasadena, CA 91125, U.S.A.

†These authors contributed equally to this work.

*Corresponding author. Email: wzhang2@caltech.edu

This file includes:

Supplementary Figures S1 to S9
Supplementary Text S1 to S5
Captions for Movies S1 to S3

Other Supplementary Materials for this manuscript include the following:

Movies S1 to S3

PEGda

DETC

DMSO

Photoresist

Si chip

Kapton spacer

Glass chip

Oil

63x objective lens

fs laser

Galvo mirror

2 μm

Blank polymer

B Metal precursor infusion

C Calcination

D Reduction

Ni-infused polymer

NiO

Ni

Air

5% H_2 /95% N_2

100s

Ni^{2+}

NO_3^-

3

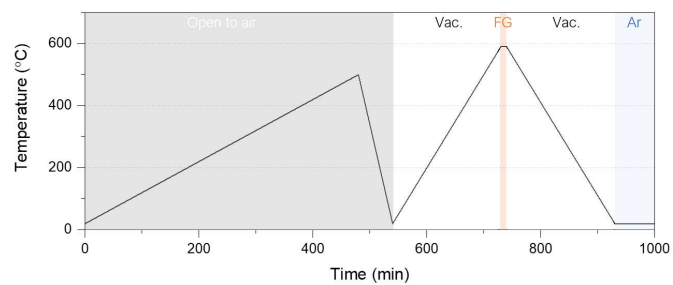


Figure S2. Thermal treatment profiles during steps (iii)-(iv). The varying background colors indicate different gas environments.

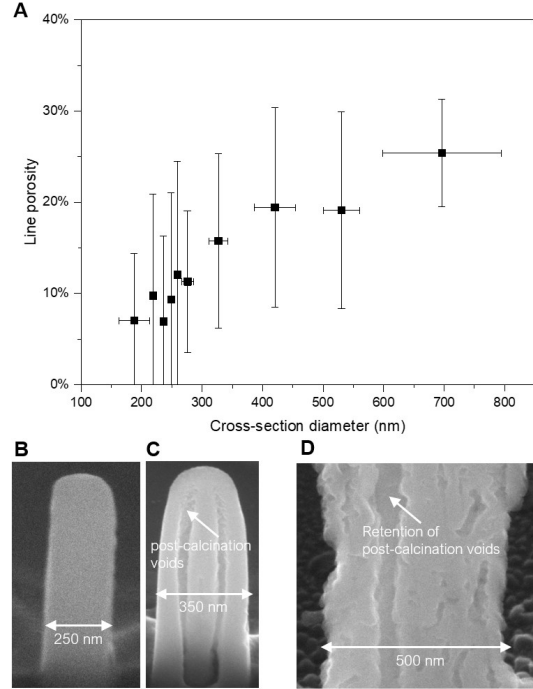


Figure S3. Porosity. (A) Porosity measured along horizontal lines on FIB-prepared vertical cross-sections of Ni pillars (see Supplementary Text S2 for measurement method). Every 17 measurements are binned into one black square for a clearer view, with error bars representing standard deviations along the corresponding axes. (B-C) SEM micrographs of NiO intermediate product, consistently showing ~fully dense microstructure at $D \lesssim 300$ nm (B) and long vertical post-calcination voids at $D \gtrsim 300$ nm; (D) SEM micrograph of Ni final product showing retention of post-calcination voids in larger pillars, in contrast to stochastically distributed pores in smaller pillars (Fig. 2C).

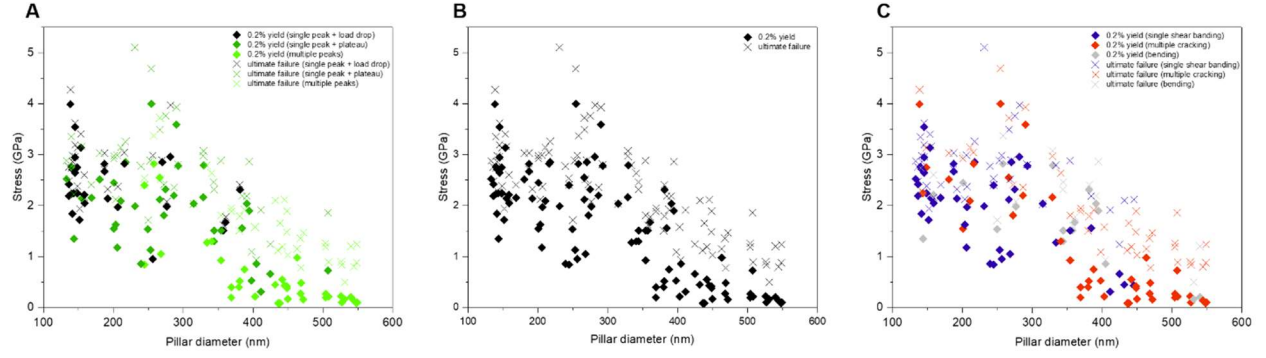


Figure S4. Ni pillar strengths as a function of the pillar diameter. (A) coloring is based on stress-strain characters; (B) uncolored; (C): coloring is based on deformation modes. Diamond symbols indicate the 0.2% yield stress, and the cross symbols indicate ultimate failure stress.

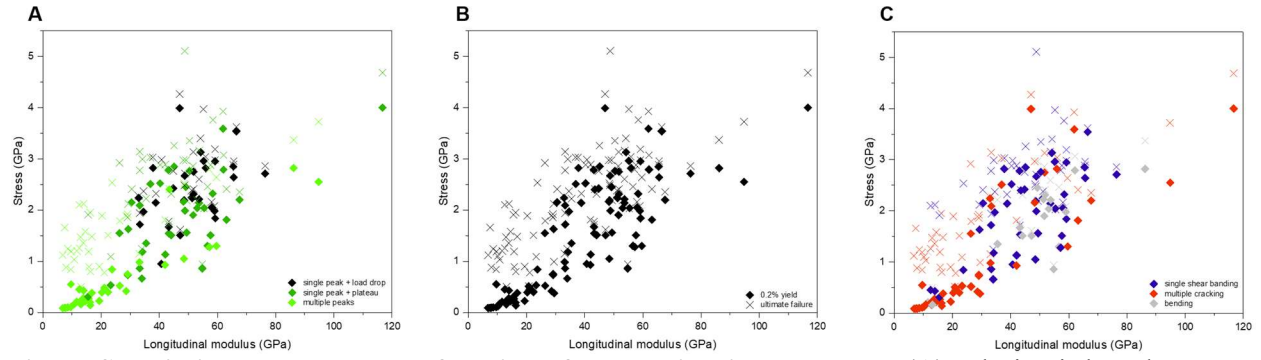


Figure S5. Ni pillar strengths as a function of the longitudinal modulus. (A) coloring is based on stress-strain characters; (B) uncolored; (C): coloring is based on deformation modes. Diamond symbols indicate the 0.2% yield stress, and the cross symbols indicate ultimate failure stress.

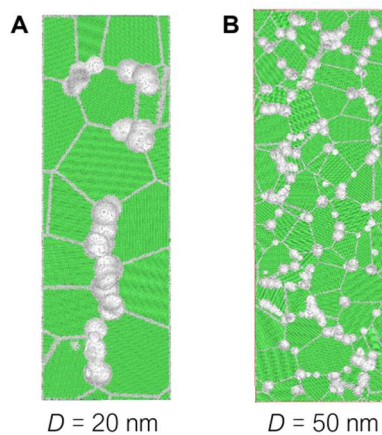


Figure S6. Initial configuration of the MD-simulated pillars in Fig. 3. Pillars of (A) 20 nm diameter and (B) 50 nm diameter. Atoms in green are of fcc coordination; atoms in white are of unknown coordination, representing grain boundaries and void surfaces.

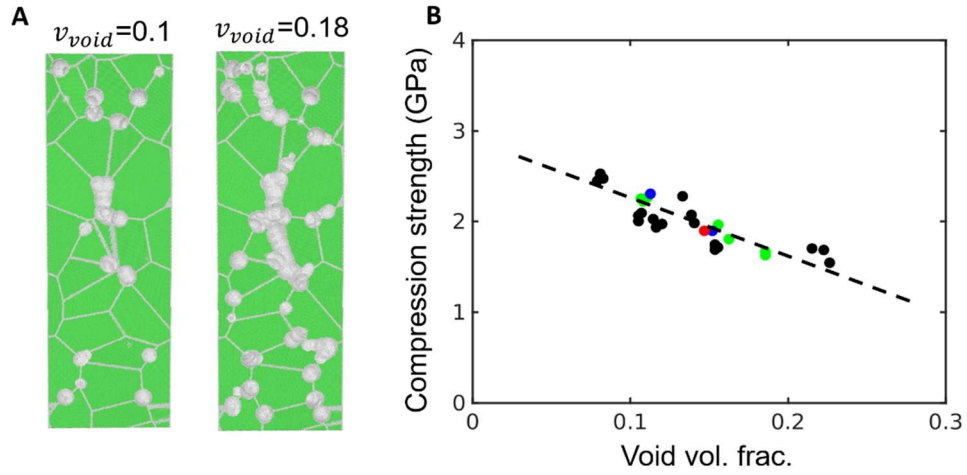


Figure S7. Effect of porosity on compression strength of Ni nanopillars. (A) Initial microstructures of typical Ni nanopillars in MD simulations with 10% and 18% porosity. Spherical voids are generated along the internal grain boundaries. Atoms with FCC and unknown coordination structures (at surface and grain boundaries) are colored green and white. (B) Compression strength of Ni nanopillars as a function of initial void volume fraction. Data points are colored by pillar diameter: 20 nm (black), 30 nm (green), 40 nm (blue) and 50 nm (red).

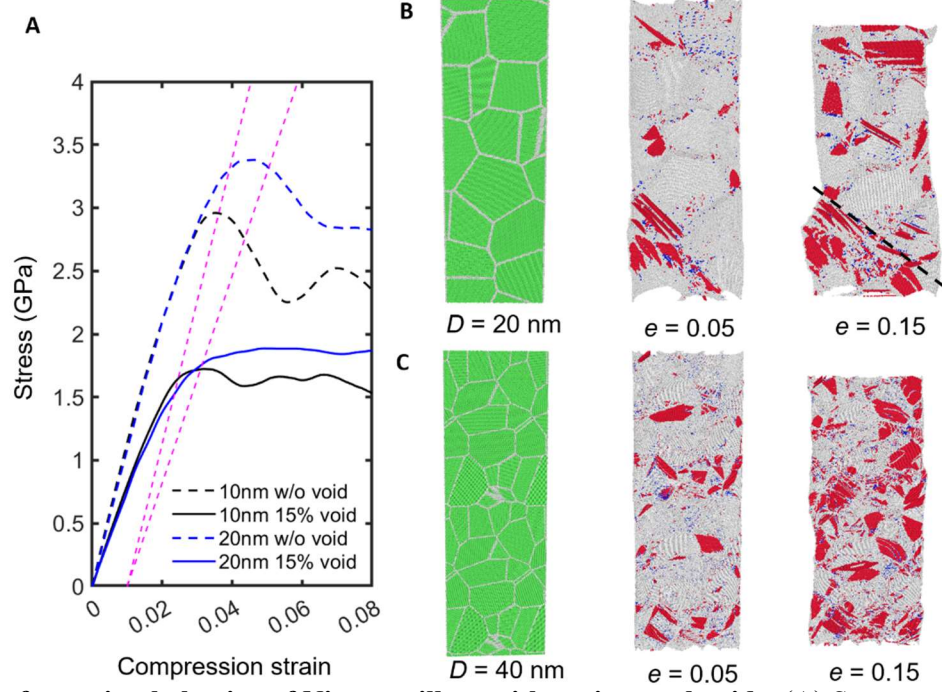


Figure S8. Deformation behavior of Ni nanopillars without internal voids. (A) Stress-strain curves of Ni nanopillars with different porosity and diameter. Dashed magenta lines show the 1% offset using elastic modulus at given porosity. Snapshots from MD simulations showing the compressive deformation process of typical Ni nanopillars with diameters of (B) 20 nm and (C) 40 nm with increasing strain. Atoms with fcc, hcp, bcc, and unknown coordination are colored green, red, blue, and white, respectively. In deformed samples, bulk fcc atoms are removed for clearer view. The dashed black line in (B) indicates the location of localized slip band.

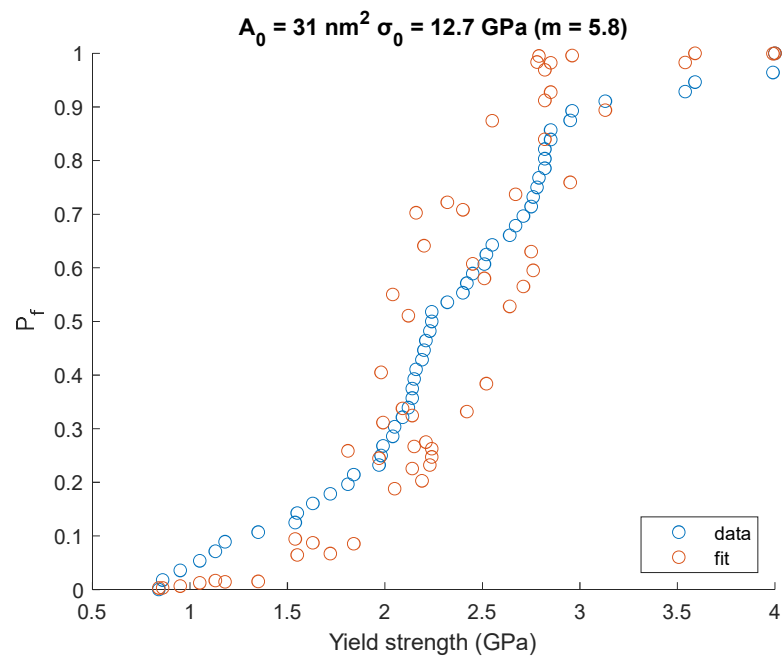


Figure S9. PWBL distribution fitting to nanopillar compression experimental results.

Supplementary Text S1. Materials and Methods.

1. Sample fabrication

We prepared customized photoresists for two photon lithography (TPL) to produce samples with pre-designed geometries. The two-photon initiator 7-diethylamino-3-thenolcoumarin (DETC, Exciton) was dissolved in dimethyl sulfoxide (DMSO, Sigma-Aldrich) at 1-mg DETC per 75- μ L DMSO. The solution was mixed with poly(ethylene glycol) diacrylate $M_n = 575$ (PEGda 575, Sigma-Aldrich) and deionized water at a volumetric ratio of 1:7.3:2.7, forming a yellow solution as the finished photoresist. TPL printing was performed on Photonic Professional GT (Nanoscribe GmbH) with a Zeiss Plan-Apochromat 63x/1.4 Oil DIC objective at a laser power of 100 mW and speed of 1.5 mm/s (Fig. S1A). Pillars (diameter = 2 μ m; aspect ratio = 3) on top of a 3 μ m-tall one-layer square lattice support were printed on Si wafers. The printed samples were then developed in deionized water for 5 minutes to form the blank hydrogel templates and subsequently submerged into a 0.002-0.05 M aqueous solution of nickel nitrate hexahydrate (99.999%, Sigma-Aldrich) at 40°C for 60 minutes (Fig. S1B) to form a Ni-infused hydrogel. Then, the samples were moved from the solution to the tube furnace (MTI OTF-1500X) for two-step thermal treatment: (i) open-to-air calcination by heating at 1°C/min to 500 °C and cooling at 3°C/min back to the room temperature (Fig. S1C); (ii) reduction by heating at 3°C/min to 590°C under vacuum, holding at 590°C for 3 min under 100-Torr forming gas (FG; 95% N₂ and 5% H₂), and cooling at 3°C/min back to the room temperature under vacuum (Figs. S1D and S2). The final product was temporarily stored in Ar environment before transferred to high-vacuum conditions for further characterizations.

2. Microstructure characterizations

Secondary electron micrographs were collected in a dual-beam focused-ion beam scanning electron microscope (FIB-SEM, Thermo Fisher Versa 3D) at the electron accelerating voltages of 10 and 20 keV. The same dual-beam instrument was used for cross-sectioning and preparing transmission electron microscope (TEM) lamellae using the focused-ion-beam (FIB) lift-out method²⁸ with a Ga-ion accelerating voltage of 30 keV and currents incrementally reduced from 5 nA to 10 pA. TEM (JEOL 2800) was conducted at 200 keV; the different crystal phases were identified based on the Fast Fourier Transformation (FFT) of relevant high-resolution TEM (HRTEM) images with visible lattice fringes using Gatan DigitalMicrograph.

Additional nanopillars, which were not used for *in situ* compression, were fabricated with the identical protocol for porosity estimation. Each cylindrical nanopillar was FIB-milled in a top-down configuration (pillar axis parallel to ion beam) to remove one semicylinder of the volume so as to expose the longitudinal cross-section (in the electron-beam view), whose vertical dimension is the pillar height, and the lateral dimension is the pillar diameter. On each cross-section, horizontal lines were drawn evenly at 5%, 15%, ..., 85%, and 95% of the pillar height: the line length corresponds to a diameter measurement, and the void length-to-total length ratio corresponds to a porosity measurement for the specific diameter. A total of $N = 170$ line porosity measurement were performed, and the diameter-to-porosity relation was summarized in Figure S3.

3. *In situ* nanomechanical experiments

Uniaxial compression of individual nanopillars was performed *in situ* using the testing system FT-NMT04 (FemtoTools AG) mounted in the SEM (Thermo Fisher Versa 3D) sample chamber under high-vacuum conditions and an electron beam voltage of 20 keV. The instrument is intrinsically displacement-driven, precluding artificial displacement bursts common in intrinsically load-driven instruments usually as a combined result of mechanical instabilities, limited load-frame stiffness, and feedback control failures. The pillar diameter, D , and height, H , were measured via SEM immediately before the compression. A 10 μ m-diameter diamond flat-punch nanoindenter tip was used for displacement-controlled tests with continuous stiffness measurement at a strain rate of 10^{-2} s⁻¹ and a data collection rate of 200 Hz for load, P , and tip displacement, Δx ; the system compliance is accounted for by the program's built-in calibration procedure. From Δx , the pillar deformation, Δx_{pillar} , was calculated by subtracting the

local nanoindenter tip and substrate deformation using the Sneddon's approach²⁹. Uniaxial engineering stress σ and strain ε were computed: $\sigma = 4P/\pi D^2$ and $\varepsilon = \Delta x_{pillar}/H$.

4. Molecular dynamics simulations

A series of large-scale molecular dynamics (MD) were performed to study the deformation behavior of nanocrystalline Ni nanopillars under uniaxial compression using the open-source code LAMMPS³⁰ and recently developed embedded atom method (EAM) potential³¹. Pristine polycrystalline pillar samples with an average grain size of 14 nm were first cut from polycrystalline rectangular prism generated using Voronoi procedure²⁰. Random nanovoids with a characteristic diameter of 4 nm were subsequently generated near the internal GBs of the pristine nanopillars samples. We generated a series of nanopillar samples containing ~2-22 million atoms with aspect ratio fixed at 3, diameter ranging from 20 nm to 50 nm, and porosity varying between 8% and 22%. Before compressive loading, the nanopillar samples were equilibrated at 300 K for 200 ps under the isothermal–isobaric (NPT) ensemble. Periodic boundary condition was adopted for the axial direction and free boundary condition was used in the radial direction. The relaxed nanopillar samples were subsequently deformed along the axial direction to a compressive strain, e , of 0.3 at a constant strain rate of $5 \times 10^8 \text{ s}^{-1}$. Dislocation structure analysis was performed and visualized using OVITO³².

Supplementary Text S2. Mechanical behavior of larger pillars (up to $D \sim 550$ nm).

As noted in Fig. S3, these larger Ni pillars contained the retained calcination-induced defects (the continuous longitudinal core-shell voids), which dominated the deformation behavior. From *in situ* compression, these pillars were found to experience significantly lower $\sigma_y \sim 0.2$ GPa and deformed via multiple cracking, agreeing with influence from the continuous longitudinal voids (Movie S3). These cracking events were reflected in the stress-strain curve as multiple peaks and load drops. By looking at a total of $N = 44$ larger pillar compression results, a much higher scaling factor was determined to be $\beta \sim 4$, suggesting the presence of more defects or increasingly more severe defects, agreeing with the increased porosity measured from pillar cross-sections (Fig. S3).

Supplementary Text S3. Limitations in using MD simulations for the present nanopillar compression experiment.

In this study, we have performed large scale MD simulations to gain atomic insights on the deformation mechanism and size effect of nanoporous nanocrystalline Ni nanopillars. While good qualitative agreement can be found between the experiments and simulations, there exist some discrepancy on the geometric parameters and quantitative results of the mechanical properties as detailed in Table S1.

Table S1. Difference in geometry and mechanical property of Ni nanopillars between the experiment and MD simulation.

	Experiment	Simulation
Grain size	30-50 nm	14 nm
Pillar diameter	130-330 nm	20-50 nm
Pore size	~30-50 nm	4 nm
Porosity	~10%	~10%-20%
Strain rates	10^{-2} s^{-1}	$5 \times 10^8 \text{ s}^{-1}$
Yielding strain	~5%	~3%
Modulus	$51 \pm 17 \text{ GPa}$	~70-100 GPa
Yield stress	1-3 GPa	1.5-2.5 GPa

Those quantitative discrepancies can be understood from the following intrinsic assumptions and constraints in our MD simulations: 1) Limitation in length scale and time scale because of computational power. In our case, our largest MD model contains 22 million atoms ($D = 50 \text{ nm}$) and is still much smaller than the smallest pillar in the experiment ($D \sim 130 \text{ nm}$). Our strain rate in the simulation is around ten orders of magnitude higher than in the experiment. The difference in length and time scales could affect a series of deformation behaviors (i.e., grain boundary sliding, dislocation nucleation/interaction), and thus shift the balance between different deformation mechanisms (i.e., grain boundary mediated plasticity vs. dislocation mediated plasticity). 2) Simplified microstructures of the simulation model. MD simulations were performed on nanopillars with relatively clean grain boundaries and spherical pores, while the grain boundary structure in the experiment might be defective with larger free volume or decorated with solutes, and the non-spherical nanopores in experiment could have higher stress concentration than the simulation model at the same porosity. The difference in grain boundary structure and pore geometry could both affect the dislocation nucleation and transmission behavior in the nanopillars. 3) Accuracy of interatomic potential. We have adopted the widely used EAM potential for Ni in our MD simulations. However, the accuracy of the dislocation nucleation energy barrier at grain boundary/free surface and dislocation core structure might not be guaranteed, which can be another error source for the discrepancy between experiments and simulations.

While we hold good confidence that the atomic mechanism revealed by our MD simulations on the transition of deformation modes (localized shear banding vs. homogenized deformation) and reduced size dependence of the yield strength of the nanopillars should function similarly in the experiments, we acknowledge that the critical pillar size for the transition and the scaling factor β in Eq. 1 could be different in simulations and experiments due to the constraints discussed above. The modulus and yield stress of the nanopillars in MD simulations both decrease with increasing porosity and are within the similar range of the values from the experiment – although greater variance is observed in experiments due to the more complex microstructures (i.e., grain boundary structure and irregular pore morphology) of the AM-fabricated nanopillars.

Supplementary Text S4. Nanopillar compression results in the context of Precursor-to-Weibull (PWBL) distribution.

We adapted the expression for the failure probability based on the PWBL distribution discussed by Bernal⁴⁶ to the present experimental results of Ni nanopillar compression:

$$P_{fj} = 1 - \left(1 - \left(\frac{\sigma_j}{\sigma_0}\right)^m\right)^{N_j}$$

where:

- (i) P_{fj} is the failure probability of pillar #j;
- (ii) σ_j is the yield strength of pillar #j measured by the experiment;
- (iii) σ_0 is the distribution parameter for characteristic stress;
- (iv) m is the distribution parameter for Weibull modulus;
- (v) N_j is the number of representative element in pillar #j: we consider the surface-mediated dislocation plasticity as the source of yielding, thus we take a 2D representative element and A_0 as the distribution parameter for the size (i.e., area) of the element; therefore, $N_j = A_j/A_0$ with A_j approximated as the cylindrical side-surface area of pillar #j.

We performed least-square fitting for $N = 56$ pillars, where the experimental value of $P_f(\sigma)$ is approximated by the proportion of tested pillars whose yield strength was $< \sigma$. Results are summarized in Figure S9, where we obtained the PWBL parameters to be: $A_0 = 31 \text{ nm}^2$, $\sigma_0 = 12.7 \text{ GPa}$, and $m = 5.8$. Note that approximating A_j using the exterior surface area is an underestimation due the surface roughness and the presence of interior pores; therefore A_0 may be underestimated as well.

Supplementary Text S5. Experimental control over microstructural dimensions and the influence on the nanopillar yield strength.

From our experience with sample fabrication, prolonging the reduction step can cause grain coarsening to > 150 nm. Meanwhile, the grain growth leads towards a morphology of faceted grains and uneven pillar diameter, where the product starts to resemble a stack of a few grains and would not be suitable for uniaxial compression.

For such microstructure, we would expect the mechanical response to resemble that of a bi-crystalline counterpart whose pillar diameter and grain size become comparable, whose yield strength (i.e., the stress required for dislocation plasticity) could be lowered as the dislocation nucleation/activation stress is in general inversely related to the free-surface radius of curvature. And this indeed has been preliminarily observed in our ongoing, unpublished work on compression of Ni nanolattices fabricated with different reduction treatment – the specimens with the coarsened grains exhibited observable decrease in yield strength.

Estimating the ligament strength using the Suquet upper bound (SU)⁵¹:

$$\sigma_y^{SU} = 6\sigma_{ys}\bar{\rho}/\sqrt{69 - 33\bar{\rho}} \quad \text{Eq. 2}$$

Where σ_{ys} represents the constituent material, i.e., individual ligaments, yield strength, and $\bar{\rho}$ represents the relative density. Using $\bar{\rho} \sim 90\%$, we obtain the ligament yield strength to be 16% higher than the pillar strength while not approaching the theoretical limit, suggesting two-fold effects of pore surfaces – (i) strengthening by dislocation escape at pore surfaces and (ii) facilitated dislocation nucleation at pore surface-GB junctions. Hakamada and Mabuchi examined the ligament yield strength-size dependence for nanoporous Au with ligament sizes of 5-126 nm using Eq. 1 and obtained $\beta = 0.20$, which they attributed to dislocation nucleation at free surfaces, supporting our present argument on pore surfaces-mediated deformation⁵⁰.

Movie S1. *In situ* SEM mechanical test on a representative Ni pillar ($D = 145$ nm). The video is at real-time speed. See Fig. 3C for pre- and post-mortem images.

Movie S2. *In situ* SEM mechanical test on a representative Ni pillar ($D = 211$ nm). The video is at real-time speed. See Fig. 3D for pre- and post-mortem images.

Movie S3. *In situ* SEM mechanical test on a large Ni pillar ($D = 508$ nm). The video is at 10x speed.